SERDP

INTERIM REPORT

Bistatic Acoustic Scattering from Munitions: Interactions with Nearby Clutter and the Water-Sediment Interface

Steven Kargl
Aubrey L. España
Applied Physics Laboratory, University of Washington

November 2020

SERDP Project MR19-1234

REPORT DOCUMENTATION PAGE

Form Approved
OMB No. 0704-0188

1. REPORT DATE *(DD-MM-YYYY)*	**2. REPORT TYPE**	**3. DATES COVERED** *(From - To)*
01/11/2020	SERDP Interim Report	8/19/2019 - 8/19/2023

4. TITLE AND SUBTITLE

Bistatic Acoustic Scattering from Munitions: Interactions with Nearby Clutter and the Water-Sediment Interface

5a. CONTRACT NUMBER
19-C-0058

5b. GRANT NUMBER

5c. PROGRAM ELEMENT NUMBER

6. AUTHOR(S)
Steven Kargl
Aubrey L. España

5d. PROJECT NUMBER
MR19-1234

5e. TASK NUMBER

5f. WORK UNIT NUMBER

7. PERFORMING ORGANIZATION NAME(S) AND ADDRESS(ES)
Applied Physics Laboratory, University of Washington
1013 NE 40th St
Seattle, WA 98105-6698

8. PERFORMING ORGANIZATION REPORT NUMBER
MR19-1234

9. SPONSORING/MONITORING AGENCY NAME(S) AND ADDRESS(ES)
Strategic Environmental Research and Development Program (SERDP)
4800 Mark Center Drive, Suite 16F16
Alexandria, VA 22350-3605

10. SPONSOR/MONITOR'S ACRONYM(S)
SERDP

11. SPONSOR/MONITOR'S REPORT NUMBER(S)
MR19-1234

12. DISTRIBUTION/AVAILABILITY STATEMENT
DISTRIBUTION STATEMENT A. Approved for public release: distribution unlimited.

13. SUPPLEMENTARY NOTES

14. ABSTRACT
The first year of MR19-1234 saw progress on four tasks: (1) bistatic scattering, (2) multiple scattering from targets in the free field, (3) frequency-dependent beam patterns, and (4) reverberation from small-scale surface roughness. Each of these tasks required modifications to or improvements in the implementation of the target-in-the-environment response (TIER) model. As part of the work on the TIER model, the numerical implementation was refactored to permit a straightforward integration of multiple scattering. These tasks are described in the following document.

15. SUBJECT TERMS
Bistatic Acoustic Scattering, Munitions, Water-Sediment Interface, UXO, Acoustic Response, Sediment Interface Scattering, TIER model, Acoustic Target Classification

16. SECURITY CLASSIFICATION OF:			**17. LIMITATION OF ABSTRACT**	**18. NUMBER OF PAGES**	**19a. NAME OF RESPONSIBLE PERSON**
a. REPORT	**b. ABSTRACT**	**c. THIS PAGE**			Steven Kargl
UNCLASS	UNCLASS	UNCLASS	UNCLASS	27	**19b. TELEPHONE NUMBER** *(Include area code)* 206-685-4677

Contents

List of Figures

List of Tables

Abstract

The first year of MR19-1234 saw progress on four tasks: (1) bistatic scattering, (2) multiple scattering from targets in the free field, (3) frequency-dependent beam patterns, and (4) reverberation from small-scale surface roughness. Each of these tasks required modifications to or improvements in the implementation of the target-in-the-environment response (TIER) model. As part of the work on the TIER model, the numerical implementation was refactored to permit a straightforward integration of multiple scattering. These tasks are described in the following document.

1 Introduction

A brief overview of the target-in-the-environment response (TIER) model is given to provide background for the progress to date. A detail description of the TIER model can be found in [1]. When the wavelength of sound is much smaller than the depth of a waveguide, acoustic scattering from a target within the waveguide may be approximated by an acoustic ray model [2]. Currently, the waveguide is a homogeneous fluid layer bounded above by air and below by a homogeneous sediment. (Relaxing the restriction of a homogeneous fluid is a task to be investigated in the second year of this project.) The sediment is assumed to be either a homogeneous attenuating fluid with a frequency-independent loss parameter [3] or a fluid described by an effective density fluid model [4]. Figure Fig. 1(a) depicts the scattering problem where the direct scattering ray path and ray paths that interact once with either the upper or lower boundary are shown. The physical source, physical receiver, and target are denoted by S_0, R_0, and T. By considering image sources and image receivers reflected through the boundaries, one can trace acoustic ray paths to these images. Figure 1(b) shows image sources and images receivers and their associated acoustic ray paths, and depicts the reduction of the waveguide scattering problem to an equivalent superposition of many free-field scattering problems.

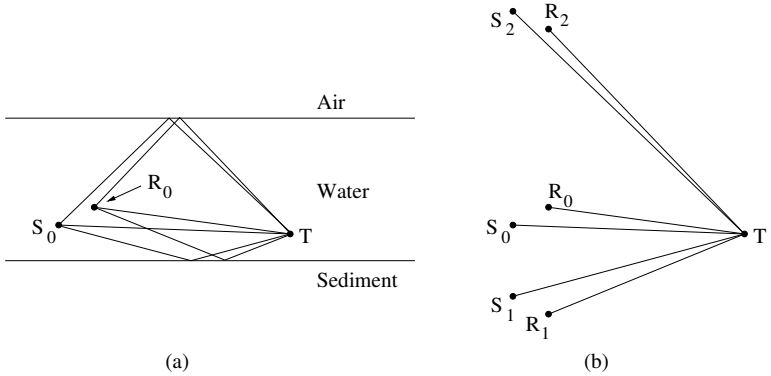

Figure 1: (a) Diagram of paths that interact at-most once with the upper and/or lower boundaries of a waveguide. (b) Equivalent superposition of free-field scattering involving image sources (S_1 and S_2) and image receivers (R_1 and R_2).

With $\boldsymbol{r}_i$, $\boldsymbol{r}_j$, and $\boldsymbol{r}_t$ representing source, receiver, and target locations in a global coordinate system, $d_{ti} = |\boldsymbol{r}_t - \boldsymbol{r}_i|$ and $d_{jt} = |\boldsymbol{r}_j - \boldsymbol{r}_t|$ are distances in a target-centered coordinate geometry. The physical source corresponds to $i = 0$ and its images have $i > 0$; while $j = 0$ denotes the actual receiver and its images have $j > 0$. For a fluid with sound speed c_1, the time delay associated with propagation from the ith source to the target is $t_{ti} = d_{ti}/c_1$; and likewise, the propagation time delay from the target to the jth receiver is $t_{jt} = d_{jt}/c_1$. The assumed time convention is $\exp(-\imath\omega t)$ with t and ω denoting time and angular frequency. The spectrum of the total scattered pressure is then

$$P(\omega) = r_0 P_{src}(\omega) \sum_{j=0} \sum_{i=0} \left[A_{jt} B_{jt}(\hat{d}_{jt}, \omega) e^{\imath\omega t_{jt}} \right] s(\hat{d}_{jt}, \hat{d}_{ti}, \omega) \left[A_{ti} B_{ti}(\hat{d}_{ti}, \omega) e^{\imath\omega t_{ti}} \right] \qquad (1)$$

where r_0 is a reference distance (typically 1 m), $P_{src}(\omega)$ is the spectrum of the transmitted signal, and time delays enter as positive phase shifts. The amplitudes $A_{jt} = U^{n_j} L^{m_j}/d_{jt}$ and

$A_{ti} = U^{n_i} L^{m_i}/d_{ti}$ account for interactions with waveguide boundaries and geometric spreading. Reflection coefficients at upper and lower boundaries are $U(\theta_g)$ and $L(\theta_g)$, where θ_g is a local grazing angle given by either $\cos\theta_i = R_{ti}/d_{ti}$ or $\cos\theta_j = R_{jt}/d_{jt}$. Here, the horizontal distances are $R_{ti} = |\boldsymbol{R}_t - \boldsymbol{R}_i|$ and $R_{jt} = |\boldsymbol{R}_j - \boldsymbol{R}_t|$ with $\boldsymbol{R} = x\hat{x} + y\hat{y}$ such that $\hat{x}$ and $\hat{y}$ are Cartesian unit vectors in the global coordinate system. The m_i, n_i, m_j, and n_j exponents indicate the number of interactions a ray has had with a given boundary. Source and receiver beam patterns are $B_{ti}(\hat{d}_{ti}, \omega)$ and $B_{jt}(\hat{d}_{jt}, \omega)$. In Eq. (1), the scattering process is encapsulated in the free-field scattering amplitude $s(\hat{d}_{jt}, \hat{d}_{ti}, \omega)$. The scattering amplitude is expressed here in terms of unit vectors for the source and receiver relative to the target location. These unit vectors are $\hat{d}_{ti} = (\boldsymbol{r}_t - \boldsymbol{r}_i)/d_{ti}$ and $\hat{d}_{jt} = (\boldsymbol{r}_j - \boldsymbol{r}_t)/d_{jt}$ for the ith source and jth receiver.

Under typical operational conditions for a short-range synthetic aperture sonar (SAS) platform, the air-water boundary can be ignored, because paths that interact with this boundary are either removed by time-gating the received signals or suppressed by the beam patterns of the source and receiver. In addition, the separation distance between the physical source and physical receiver is much smaller than d_{ti} and d_{jt}, so the source and receiver can be considered to be co-located. Under these conditions, only four ray paths associated with the actual source and receiver and their images in the sediment contribute to the scattered pressure (i.e., $i = 0, 1$ and $j = 0, 1$) [5]. For simplicity, we set $d_0 = d_{t0} = d_{0t}$ and $d_1 = d_{t1} = d_{1t}$, which gives the spectrum for the scattered pressure as

$$P(\omega) = r_0 P_{src}(\omega) \left[s_1 \frac{\exp(\imath\omega t_0)}{d_0^2} + 2L(\theta_g) s_2 \frac{\exp(\imath\omega t_1)}{d_0 d_1} + L^2(\theta_g) s_3 \frac{\exp(\imath\omega t_2)}{d_1^2} \right] \tag{2}$$

with $t_0 = 2d_0/c_1$, $t_1 = (d_0 + d_1)/c_1$, $t_2 = 2d_1/c_1$, and grazing angle θ_g. The reflection coefficient for a fluid-like sediment is

$$L(\theta_g) = \frac{\rho \sin\theta_g - (\kappa^2 - \cos^2\theta_g)^{1/2}}{\rho \sin\theta_g + (\kappa^2 - \cos^2\theta_g)^{1/2}}, \tag{3}$$

where $\rho = \rho_2/\rho_1$, $\kappa = k_2/k_1 = (1 + \imath\delta)/\nu$, and $\nu = c_2/c_1$ is a real index of refraction. Here, c_2, ρ_2, and δ are the sound speed, density, and loss parameter for the sediment, respectively. The scattering amplitudes are $s_1 = s(\hat{d}_0, -\hat{d}_0, \omega)$, $s_2 = s(\hat{d}_0, -\hat{d}_1, \omega)$, and $s_3 = s(\hat{d}_1, -\hat{d}_1, \omega)$, which depend on polar and azimuthal angles for the source and receiver in the target-centered coordinate system. An inverse Fourier transform of $P(\omega)$ then gives a generated sonar signal that includes the four primary acoustic paths for a target near the seafloor. The first term within the brackets of Eq. (2) is the direct path with ray diagram $S_0 \to T \to R_0$. This path corresponds to scattering from an isolated target in the free field. The second term includes the two paths that interact once with the bottom (i.e., $S_0 \to T \to R_1 + S_1 \to T \to R_0$). These paths are reciprocal and are associated with bistatic scattering within a vertical plane perpendicular to the seafloor. The last term is a backscattering path with two bottom interactions ($S_1 \to T \to R_1$).

2 Bistatic Scattering Amplitude

The formulation of the TIER model reduced the scattering from an object in a waveguide to a superposition of free-field scattering problems. A single contribution to the total spectrum of the scattered pressure from Eq. (1) is

$$P_{ji} = \left[A_{jt}B_{jt}(\hat{d}_{jt},\omega)e^{\imath\omega t_{jt}}\right] s(\hat{d}_{jt},\hat{d}_{ti},\omega) \left[A_{ti}B_{ti}(\hat{d}_{ti},\omega)e^{\imath\omega t_{ti}}\right]. \tag{4}$$

This section describes the current progress in generalizing the numerical implementation to permit bistatic scattering from an object. Figure 2 depicts a target-centered, spherical, coordinate system for a finite cylindrical object. Due to the symmetry of this object, the coordinate system can be selected such that the axis of symmetry lies along the z-axis and the physical source is constrained to the xz-plane. The polar angle for the physical source is θ_s and for a physical receiver with an arbitrary location the polar and azimuthal angles are θ_r and φ_r. In

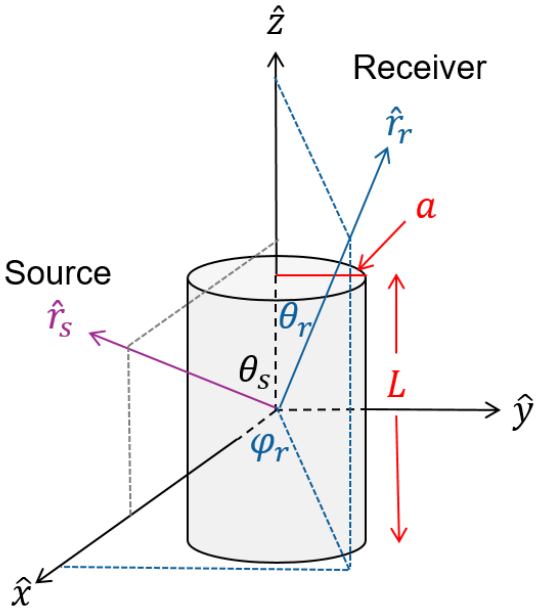

Figure 2: The target-centered coordinate system used in bistatic scattering from axisymmetric objects.

much of the previous UXO research performed by APL-UW, the physical source and physical receiver were assumed to be co-located and the object was near the water-sediment boundary (e.g., sitting proud on the surface). Under these conditions, the physical source and physical receiver have $\theta_r \equiv \theta_s$ and $\varphi_r \equiv 0$, which yields $s(\theta_s, 0, \omega)$. For a physical source and an image receiver reflected through the water-sediment boundary, one has bistatic scattering restricted to a vertical plane, which is perpendicular to the water-sediment boundary. This leads to $\theta_r \approx \theta_s$ and $\varphi_r \neq 0$, which leads to $s(\theta_s, \varphi_r, \omega)$. For objects other than spheres [6–8] and approximations for finite cylinders [9–11], the TIER model has utilized a table-driven approach with $s_{ikl} = s(i\Delta\theta, k\Delta\varphi, l\Delta f)$ with $i = 0, 1, \cdots, I$; $k = 0, 1, \cdots, K$; and $l = 0, 1, \cdots, L$. The tables are constructed in terms of the actual frequency f instead of the angular frequency ω. Prior

to SERDP MR19-1234, tables for a 2:1 aluminum cylinder (i.e., 1-ft diameter, 2-ft length), 2:1 aluminum pipe with 3/8-in wall thickness, air-filled and water-filled 105-mm artillery shell, air-filled and water-filled 155-mm howitzer shells, a scuba tank, and aluminum and steel replicas of a 100-mm projectile were constructed. These tables have $\Delta\theta = \Delta\varphi = 1^\circ$ or 2°, and $\Delta f = 100$ or 200 Hz. Recently, downward-looking sonar platforms have been deployed by APL-UW and the Applied Research Laboratory at Pennsylvania State University. There platforms can have significant separation distances between sources and receivers, and hence, an assumption of co-located source and receiver needs to be revisited. This then means $\theta_s \neq \theta_r$ and the tabulated scattering amplitude expands from a three-dimensional table to four dimensions, i.e., $s_{ijkl} = s(i\Delta\theta_s, j\Delta\theta_r, k\Delta\varphi, l\Delta f)$ with $j = 1, 2, \cdots, J$.

The generation of a table is a two-step process. First, the hybrid model [1], which combines a finite-element model for an object's elastic response and a Helmholtz propagation model, is executed after selecting $i\Delta\theta_s$ and $l\Delta f$. The scattered pressure at some range, r, is then predicted for all combinations of $j\Delta\theta_r$ and $k\Delta\varphi$. Second, the scattered pressure is converted to a normalized scattering amplitude by removing spherical spreading and compensating for the phase associated with range r:

$$s_{ijkl} = \frac{2r}{a}\frac{p_{ijkl}}{p_0}\exp[-\imath 2\pi(l\Delta f/c_1)r]. \tag{5}$$

Here, a is a characteristic dimension of the object; p_{ijkl} is the scattered pressure from the hybrid model; and, p_0 is the amplitude of the incident pressure set during the hybrid model simulation. The top line of Table 1 shows the dimensions and size of the table created for the 2:1 aluminum cylinder when the source and receiver are co-located. Each entry in the table is a 64-bit complex value, which occupies 8 bytes. The polar angle of the source satisfies $0^\circ \leq \theta_s \leq 180^\circ$ and an image receiver's azimuthal angle satisfies $-180^\circ \leq \varphi \leq 180^\circ$. The frequencies are within $1 \leq f \leq 30$ kHz, which covers the range of frequency of the LFM signal used in APL-UW experiments.

I	J	K	L	Size (MB)	Comment
181	c-l	361	291	145	full simulation
181	c-l	361	291	57	full simulation, scaling, compression
91	91†	361†	291	73	up-down symmetry
91	91†	361†	291	27	up-down symmetry, scaling, compression

Table 1: Dimensions for various generated tables for a 2:1 aluminum cylinder are shown. The fifth column is the nominal file size in megabytes (MB). Here, c-l indicates a co-located receiver. † *The table dimensions do not reflect an underlying coordinate transform from the hybrid model to the TIER model, but cylindrical symmetry is implied.*

A move from co-located source and receiver with a 3-dimensional table to an arbitrary receiver location leads to a 4-dimensional table, which would be a significant increase in file size and memory requirements during a simulation. The second line in Table 1 shows the dimensions and file size when the real and imaginary parts of the complex-valued s_{ijkl} (8 bytes) is scaled and converted to two 16-bit signed integers (4 bytes). This provides an immediate reduction from 145 MB to 72.5 MB. The final file size of 57 MB is obtained from applying

a compression algorithm to the table. It is noted that the scaling and conversion to integers reduces the relative dynamic range of simulated data from 144 dB to approximately 90 dB.

The third and fourth lines in Table 1 are the results when bistatic scattering is allowed. To ensure adequate computational resources are available, tables are not expanded to four dimensions. Rather, individual 3-dimensional tables for each of the θ_s values are constructed (e.g., 91 tables for the example here). In addition to the cylindrical symmetry, inspection of Fig. 2 reveals an up-down symmetry along the z-axis. For example, when $\theta_s = 92°$, a simulation uses the table for $\theta_s = 88°$, where the indexing into the φ dimension is flipped. Using up-down symmetry, scaling into a signed integer representation, and compressing the table results in a 81% reduction in file size (i.e., 27 MB compared to 145 MB), and with 91 files, these files occupy approximately 2.4 GB of disk space compared to 12.9 GB.

During a TIER model simulation with a given source-receiver pair, θ_s is determined and it rarely matches a tabulated $i\Delta\theta$ value, so two tables are loaded into memory. The loading process, decompresses the data and converts the scaled, signed-integer representation back to a complex-valued scattering amplitude. For example, if $\theta_s = 23.2°$, then the tables for 23° and 24° are loaded. Interpolation methods are then used to evaluate the required $s(\theta_s = 23.2°, \theta_r, \varphi, \omega)$. In the original implementation, pairs of tables were loaded on an as-needed basis. In the second-order multiple scattering example involving two 2:1 aluminum cylinders discussed in Sec. 3, moving from the first source-receiver pair to the second pair, the tables are used in the following order: $(23°, 24°)$, $(23°, 24°)$, $(45°, 46°)$, $(22°, 23°)$, $(22°, 23°)$, $(45°, 46°)$, $(15°, 16°)$, $(15°, 16°)$, $(89°, 90°)$, $(15°, 16°)$, $(15°, 16°)$, and $(89°, 90°)$. The tables, associated with the red angles, are already loaded in memory, and so new tables are not needed and therefore not re-read from disk. The blue angles cause the tables for the preceding red angles to be flushed from memory, and then the tables for the blue angles are loaded. Finally, the tables for the blue angles are flushed from memory when the following black angles are loaded into memory. In summary, several tables are re-read from disk and converted to the complex-valued scattering amplitudes multiple times in simply moving from one source-receiver pair to the next in a SAS simulation.

A least-recently-used (LRU) caching scheme has been implemented where up to ten tables are saved. When a pair of angles has been determined, if the tables are already in memory, those tables are used. If a table is not currently in the cache and a cache slot is available, then a cache slot is allocated and the table is loaded from disk. During the loading process a reference count for each cache entry is incremented. If a table is not currently in cache and no cache slots are available, then the reference counts are checked and the LRU entry is removed from the cache and a new table is loaded. For the angles listed in the example of the previous paragraph, under this caching scheme, the corresponding tables are loaded once. For the multiple scattering examples in Sec. 3 for two 2:1 aluminum cylinders, the file loading is summarized in Table 2. The reduction in file loads represents a significant decrease in computation time.

Circular SAS simulations have been performed as an initial test for the new indexing scheme into the set of tables for a bistatic scattering amplitude. A 2:1 aluminum cylinder is placed at the center of a 15-m circular path with its center located at (15,0,0.1524) m. Co-locate, omnidirectional source and receiver are scanned with an elevation of $z = 4$ m. The density and sound speed in water are $\rho_1 = 1000$ kg/m^3 and $c_1 = 1530$ m/s. For the half-space simulation, where the cylinder is proud on a medium-sand sediment, the sediment's density, sound speed, and loss parameters are $\rho_2 = 1800$ kg/m^3, $c_2 = 1694$ m/s, and $\delta = 0.008$. Comparisons

Order	Uncached	Cached
First	214	106
Second	3208	156
Third	8006	207
Fourth	14442	207

Table 2: The number of tables loaded from disk are shown. Under the original scheme, only previously loaded tables were re-used if the next θ_s could utilized the already loaded table. Under the new caching scheme and with a multiple scattering test from Sec. 3, the number of file loads is significantly reduced.

of individual pings from the simulations are shown in Fig. 3. The black line results from a simulation using the original scattering amplitude for a monostatic configuration. The red line is obtained from a simulation that utilizes the new bistatic scattering amplitudes, where the source and receiver are co-located. The minor deviation of the red line from the black is attributed to the interpolation schemes used with the various tables, and possibly the discrete resolution of the tables. Figure 4 shows SAS images for free-field and half-space circular SAS simulations. For Figs. 4(a) and 4(b) only a single contribution in Eq. (1) is computed at each

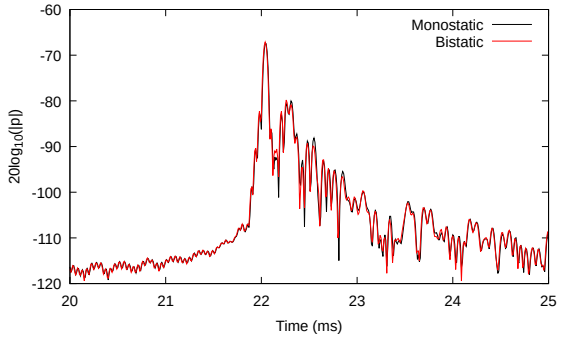

(a) Free-field scattering, 0° pose angle

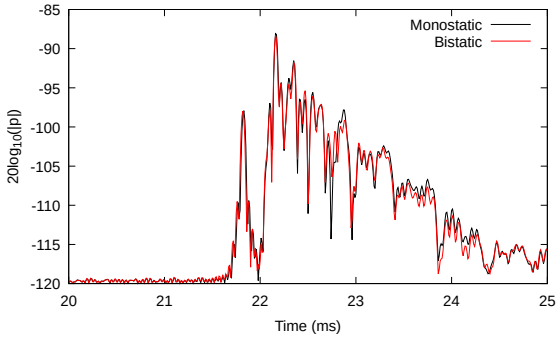

(b) Free-field scattering, 45° pose angle

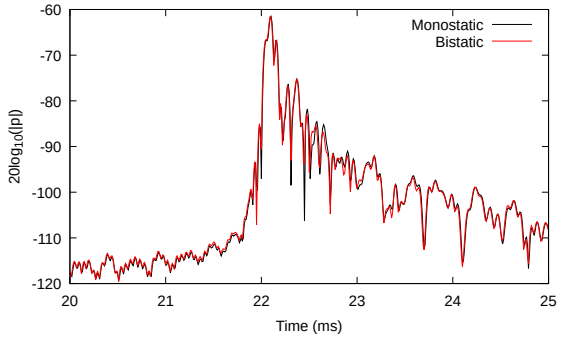

(c) Half-space scattering, 0° pose angle

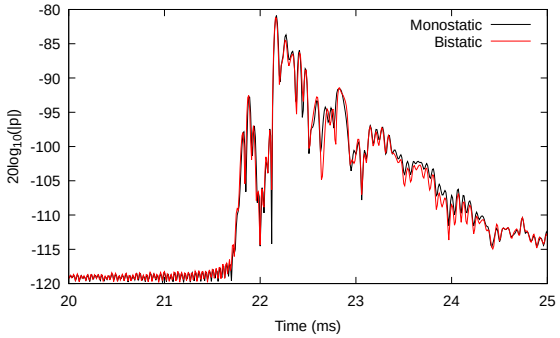

(d) Half-space scattering, 45° pose angle

Figure 3: The axis of symmetry of the cylinder is aligned with the y-axis of the global coordinate system with a 0° pose angle. A 45° pose angle is a rotation of the target such that it has a 45° orientation with respect to the y-axis.

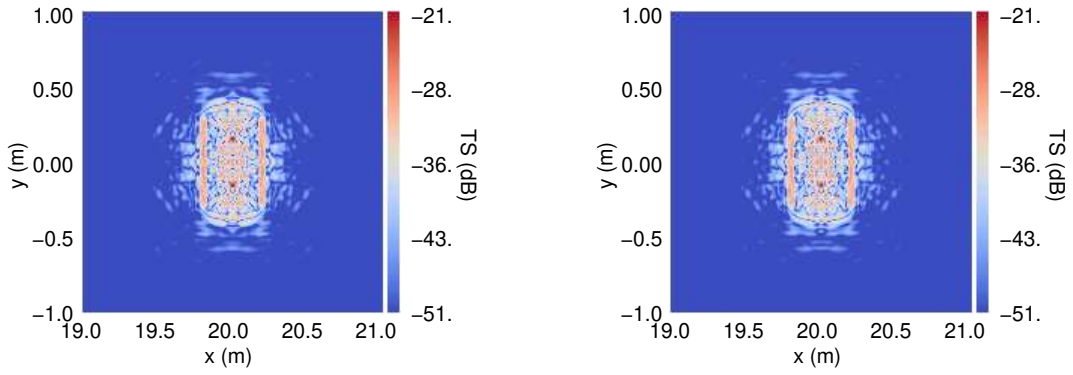

(a) Free-field Monostatic

(b) Free-field Bistatic

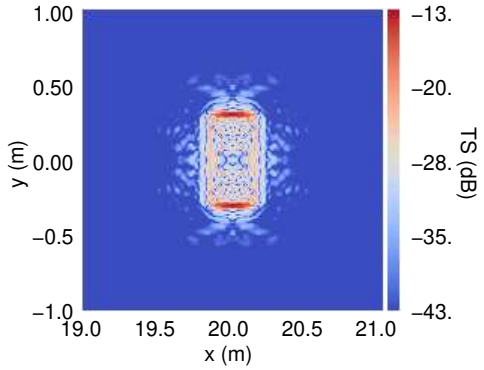

(c) Half-space Monostatic

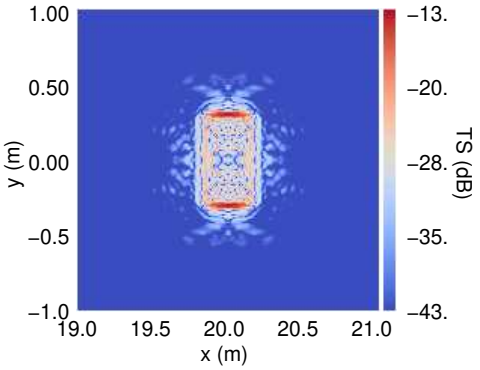

(d) Half-space Bistatic

Figure 4: (a) and (c) use the original monostatic scattering amplitude in the TIER model. (b) and (d) use the tables for bistatic scattering amplitudes.

of the 360 source/receiver locations along the circular path. For Figs. 4(c) and 4(d), an image source and image receiver reside within the sediment, which leads to four contributions.

In Figs. 3 and 4, the source and receiver were co-located. The results indicate, that at least in this special case, the original table for the scattering amplitude and the new tables for the bistatic scattering amplitudes give essentially the same target response. Figure 5 depicts the circular SAS images when the receiver leads the source by a 20° angular separation. Although circular SAS simulations from an independent model are unavailable for comparisons, the general dimensions of the imaged cylinder agree with those the 2:1 aluminum cylinder. In addition, Fig. 5 compares favorably with Fig. 4.

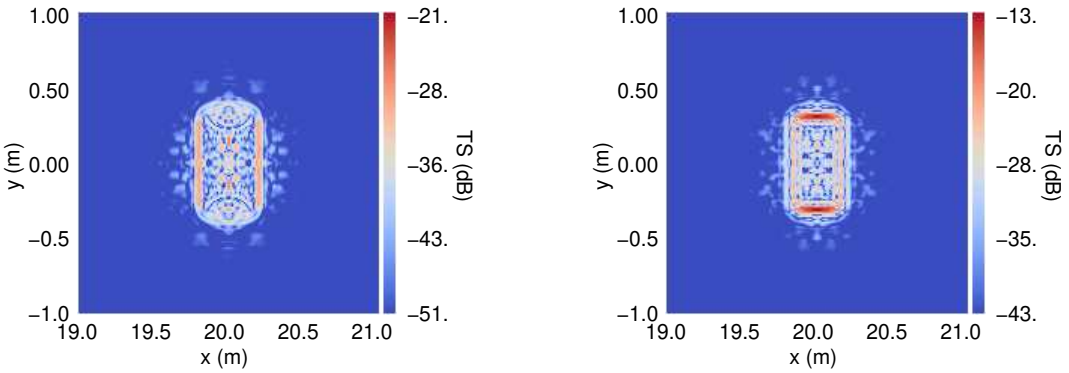

(a) Free-field

(b) Half-space

Figure 5: The source and receiver are not co-located for the simulations. (a) The free-field result includes a single contribution in Eq. (1). (b) The half-space result includes four contributions, which arise from an image source and image receiver.

3 Multiple Scattering

The development of the TIER model assumed that objects are sufficiently isolated from nearby objects that multiple scattering effects can be ignored. During CLUTTEREX17, data were collected from collections of objects, which were randomly distributed on a small area of the seafloor. The minimum separation distances between objects approached approximately 1 m for some measurements. Comparison of SAS images with diver-recorded video surveys of these random target fields found features in SAS images where no objects could be found. Hence, the assumption of isolated objects no longer holds.

An initial investigation into multiple scattering from the deployed objects requires modification to the TIER model. Recall that Eq. (1) casts the scattering from an isolated object in a waveguide into a superposition of free-field scattering from an isolated object, where one has not only the physical source and physical receiver but possibly image sources and image receivers. A single contribution to the total spectrum from Eq. (1) for the ith source and jth receiver is

$$P_{ji} = \left[A_{jt}B_{jt}(\hat{d}_{jt},\omega)e^{\imath\omega t_{jt}}\right] s(\hat{d}_{jt},\hat{d}_{ti},\omega) \left[A_{ti}B_{ti}(\hat{d}_{ti},\omega)e^{\imath\omega t_{ti}}\right]. \tag{6}$$

The quantity in the right-hand square bracket represents the propagation from a source to an object and the left-hand square bracket accounts for propagation from an object to a receiver. For an isolated object, $s(\hat{d}_{jt},\hat{d}_{ti},\omega)$ is the scattering amplitude, which contains all information about an object and the directionality of the scattered pressure. To account for possible multiple scattering effects, the scattering amplitude is replaced by an *effective* scattering amplitude such that Eq. (6) becomes

$$P_{ji}^{(n)} = \left[A_{jt}B_{jt}(\hat{d}_{jt},\omega)e^{\imath\omega t_{jt}}\right] s^{(n)}(\omega) \left[A_{ti}B_{ti}(\hat{d}_{ti},\omega)e^{\imath\omega t_{ti}}\right] \tag{7}$$

where the superscript (n) with $n > 0$ denotes the order of multiple scattering. If the objects are sufficiently isolated from each other, then $n = 1$ and the spectrum of the scattered pressure reduces to Eq. (1). A ray diagram for an isolated object has been discussion in Sec. 1, and can be expressed here as $S_i \to T_k \to R_j$ for ith source and jth receiver, and the subscript k denotes the kth object in the collection of objects. Second-order multiple scattering has $n = 2$ and involves two objects. The ray diagram is then modified to include the propagation from the kth target to lth target such that one has $S_i \to T_k \to T_l \to R_j$. It is assumed that the pressure scattered by a portion of the kth target does not interact with any other portion of the kth object. Or, if there is a self interaction, it is incorporated within the scattering amplitude of an object in isolation. This then implies the condition $k \neq l$ when summing all contributions to the total pressure. For second-order multiple scattering, Eq. (7) becomes

$$P_{ji}^{(2)} = \left[A_{jl}B_{jl}(\hat{d}_{jl},\omega)e^{\imath\omega t_{jl}}\right] s^{(2)}(\omega) \left[A_{ki}B_{ki}(\hat{d}_{ki},\omega)e^{\imath\omega t_{ki}}\right], \tag{8}$$

$$= \left[A_{jl}B_{jl}(\hat{d}_{jl},\omega)e^{\imath\omega t_{jl}}\right] s(\hat{d}_{jl},\hat{d}_{lk},\omega)\frac{\exp(\imath\omega t_{lk})}{|\boldsymbol{r}_l - \boldsymbol{r}_k|} s(\hat{d}_{lk},\hat{d}_{ki},\omega) \left[A_{ki}B_{ki}(\hat{d}_{ki},\omega)e^{\imath\omega t_{ki}}\right], \tag{9}$$

where the subscript t in Eq. (7), which represents a generic object, is replaced by an object's subscript k or l. The unit vectors point long the direction of propagation. For example, propagating from the ith source to the kth object has $\hat{d}_{ki} = (\boldsymbol{r}_k - \boldsymbol{r}_i)/d_{ki}$. The scattering amplitude, $s(\hat{d}_{lk},\hat{d}_{ki},\omega)$, is for sound from the ith source being incident on the kth object with

scattering from the kth object towards the lth object. The propagation time delay between the kth and lth objects is $t_{lk} = d_{lk}/c_1$. The scattering amplitude, $s(\hat{d}_{jl}, \hat{d}_{lk}, \omega)$, is for sound from the kth object being incident on the lth object with scattering from the lth object towards the jth receiver. It is note that the geometric spreading factor $|\boldsymbol{r}_l - \boldsymbol{r}_k|^{-1}$ is only included in Eq. (9) if it exceeds 1 m. Finally, in Eq. (9), there is an implicit double summation over all objects (i.e., $\sum_k \sum_{l \neq k}$).

The TIER model traces the time-of-flight of a wave packet along ray paths from a source to a receiver. The ray diagrams for the 4 lowest orders of multiple scattering are

$$S_i \rightarrow T_k \rightarrow R_j \qquad\qquad\qquad\qquad 1^{\text{st}} \text{ order} \tag{10}$$

$$S_i \rightarrow T_k \rightarrow T_l \rightarrow R_j \qquad k \neq l \qquad 2^{\text{nd}} \text{ order} \tag{11}$$

$$S_i \rightarrow T_k \rightarrow T_l \rightarrow T_m \rightarrow R_j \qquad k \neq l, l \neq m \qquad 3^{\text{rd}} \text{ order} \tag{12}$$

$$S_i \rightarrow T_k \rightarrow T_l \rightarrow T_m \rightarrow T_n \rightarrow R_j \qquad k \neq l, l \neq m, m \neq n \qquad 4^{\text{th}} \text{ order} \tag{13}$$

where each subscript is associated with summation over the collection of targets with the noted restrictions. These orders have been included in the TIER model. Additional orders could be added, but the accumulation of propagation time delay places the higher-order multiple scattering contributions later in time, which means the contribution may be time-gated out.

For a simple test, which eliminates any possible elastic response for an object, three unit-amplitude, rigid, point scatterers are placed at (10,4,0) m, (10,5,0) m, and (10,5.5,0) m (denote these by T_1, T_2, and T_3, respectively). The source and receiver apertures are scanned along the y-axis where the apertures are 20×20 cm^2 rectangular, frequency-dependent apertures (see Sec. 4). The apertures are scanned from (0,0,0) m to (0,10,0) m with $\Delta y = 0.025$ m. The sound speed in the water is $c_1 = 1530$ m/s. Figure 6 shows the results of including the different orders of multiple scattering. Figures 6(a) and 6(b) are those that one expects from treating the scatterers as being isolated (i.e.. using Eq. (1)). Weak observables are seen between T_2 and T_3, which is simply a result of constructive (and/or destructive) interference of the scattered pressure from the isolated targets. The second row of Fig. 6 depicts second-order multiple scattering, where 6 target arcs are seen in the magnitude of the pulse-compressed signals, and 6 prominent observables are seen in the SAS image. The point scatterers are omnidirectional, and by construction certain multiple scattering paths overlap. The observables near (10.25,5.2), (10.5,4.4), and (10.7,4.7) are associated with $(S \rightarrow T_2 \rightarrow T_3 \rightarrow R) + (S \rightarrow T_3 \rightarrow T_2 \rightarrow R)$, $(S \rightarrow T_1 \rightarrow T_2 \rightarrow R) + (S \rightarrow T_2 \rightarrow T_1 \rightarrow R)$, and $(S \rightarrow T_1 \rightarrow T_3 \rightarrow R) + (S \rightarrow T_3 \rightarrow T_1 \rightarrow R)$, respectively. It is noted that at the level of approximation made, T_2 does not obstruct the paths between T_1 and T_3. The final two rows of Fig. 6 depict third- and fourth-order multiple scattering. While it is possible to associate particular ray paths with specific observables in Figs. 6(e) and 6(h), it is not pursued here. Finally, the SAS images indicate that as the order of multiple scattering increases the observables appear further from the true location of an object and the observable is spread out in cross range. This is due to the increased time delay, which when processed by a SAS algorithm, appears as a phase shift and hence is attributed to a more removed object.

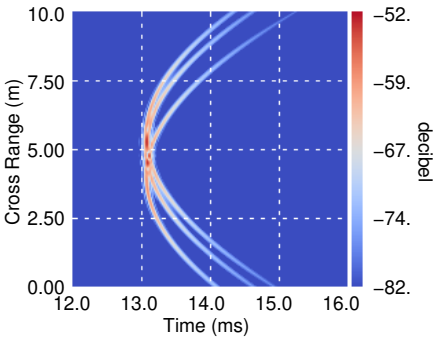

(a) Time signatures for 1^{st} order

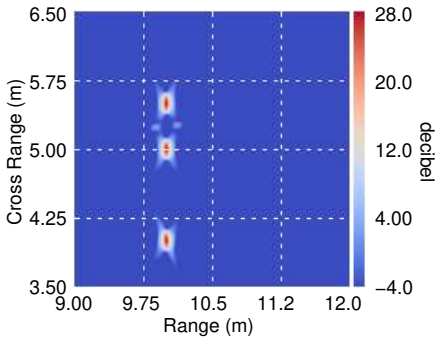

(b) SAS image for 1^{st} order

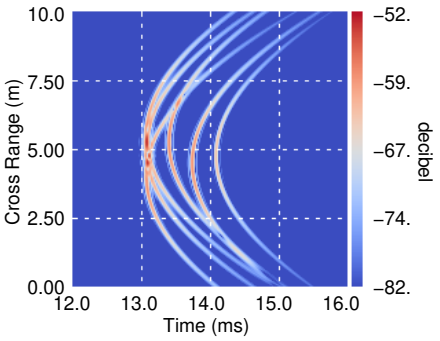

(c) Time signatures for 2^{nd} order

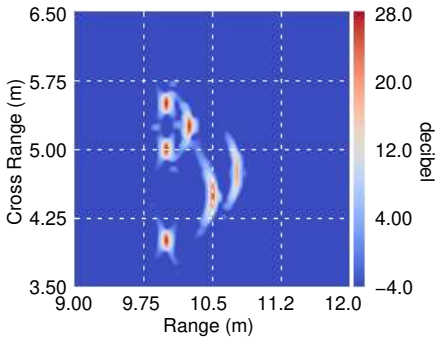

(d) SAS image for 2^{nd} order

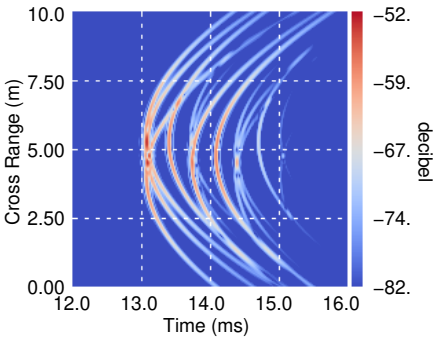

(e) Time signatures for 3^{rd} order

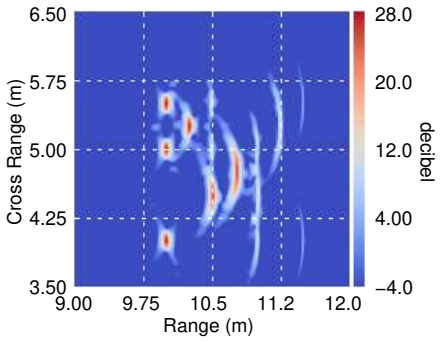

(f) SAS image for 3^{rd} order

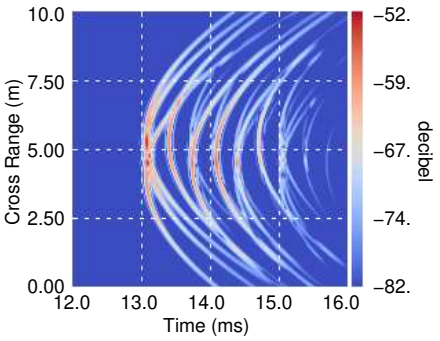

(g) Time signatures for 4^{th} order

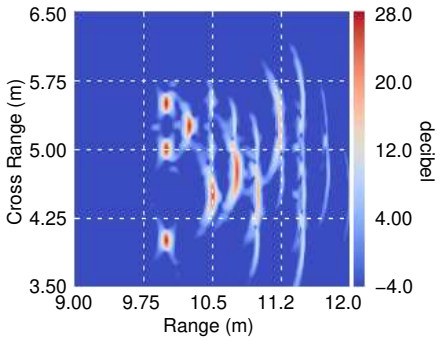

(h) SAS image for 4^{th} order

Figure 6: (a,c,e,g) Magnitude of the pulse-compressed time signatures are depicted. (b,d,f,h) SAS images created from the time signature at left.

The point scatterers considered in Fig. 6 do not include elastic responses. For elastic objects, multiple scattering requires bistatic scattering amplitudes (see Sec. 2). Tabulated bistatic scattering amplitudes are available for a 2:1 solid aluminum cylinder. Simulations were performed for cylinders at $T_1 = (10, 4.25, 0)$ m and $T_2 = (10, 5.75, 0)$ m. The source and receiver apertures are defined as those used in the simulations for Fig. 6. Object T_1 has a broadside orientation, $0°$, with respect to the path of the source and receiver (i.e., the symmetry axis of the cylinder is parallel to y-axis). Object T_2 has a $-45°$ pose with respect to broadside. In Figs. 7(a) and 7(b), one sees the time signatures and SAS image when no interaction between the aluminum cylinders occurs. The time signatures contain sufficient structure that assignment of portions of the time signatures to one or the other object is difficult (especially, compared to the point scatterer results in Figs. 6(a) and 6(b)). Synthetic aperture decomposition (SAD), used in previous SERDP projects, can be applied to the complex SAS image to isolate the time signatures in Fig. 7(a). The second row in Fig. 7 introduced second-order multiple scattering, and it is evident in the SAS image that new observable structure appears near (10.5,5). This structure is about 15 dB down from the peak response. The third row in Fig. 7 now includes both second- and third-order multiple scattering. Third-order multiple scattering contributes easily identifiable structure in both the time signatures and SAS image. In particular, the new observable in the SAS image, Fig. 7(f), is as strong as most of the target strength of the isolated object T_2 in Fig. 7(b). The last row in Fig. 7 includes fourth-order multiple-scattering, which appears to contribute little to the overall response.

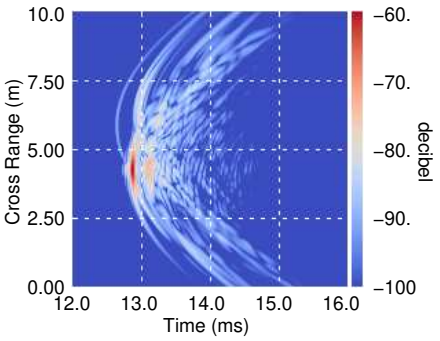

(a) Time signatures for 1^{st} order

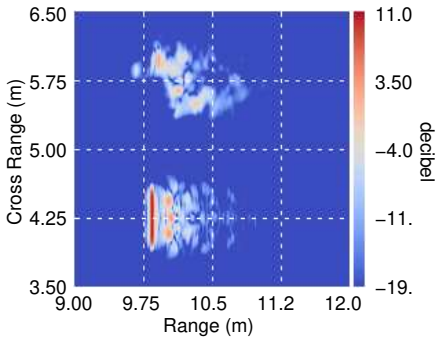

(b) SAS image for 1^{st} order

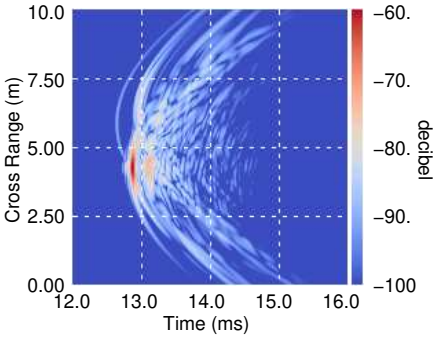

(c) Time signatures for 2^{nd} order

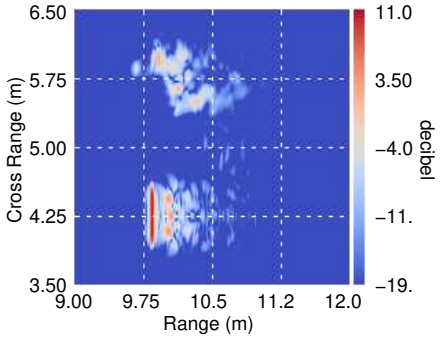

(d) SAS image for 2^{nd} order

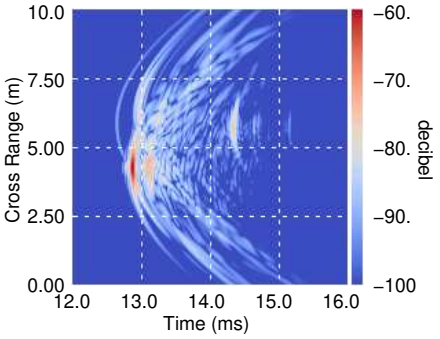

(e) Time signatures for 3^{rd} order

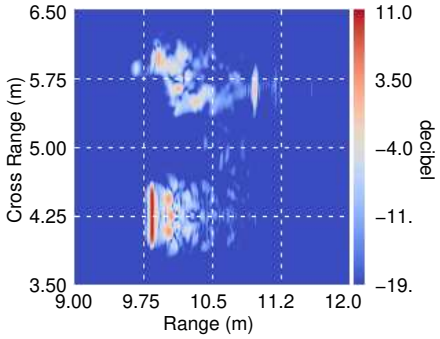

(f) SAS image for 3^{rd} order

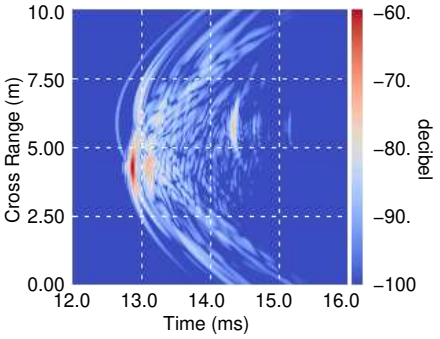

(g) Time signatures for 4^{th} order

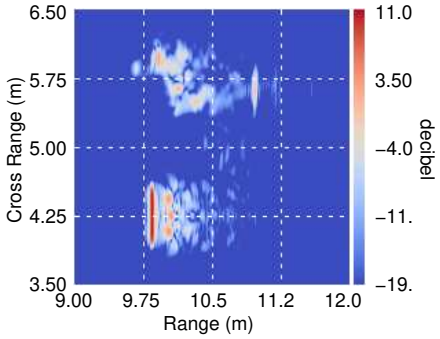

(h) SAS image for 4^{th} order

Figure 7: (a,c,e,g) Magnitude of the pulse-compressed time signatures are depicted. (b,d,f,h) SAS images created from the time signature at left.

4 Frequency-dependent Beam Pattern

The original formulation of the TIER model was developed to gain physical insight into data collected during several field measurements performed by APL-UW under ONR and SERDP funded projects. These field measurements included PONDEX10, TREX13, BAYEX14, and CLUTTEREX17, where a sonar platform was scanned along a fixed, straight rail to collect SAS data. The source deployed in those measurements was an array with effectively four elements. These elements were driven by the linear-frequency-modulated (LFM) signals depicted in Fig. 8(a) to achieve a uniform horizontal beam pattern over the entire 1-30 kHz frequency band of the source (see Fig. 8(b)). The intended beam pattern was that of a rectangular source with a 20-cm horizontal width operated at 15-kHz (i.e., the carrier frequency of the LFM signal), which is the green curve in Fig. 8(c). The magenta and cyan curves in Fig. 8(c) are the beam patterns for a 20-cm rectangular source driven at 3 and 30 kHz.

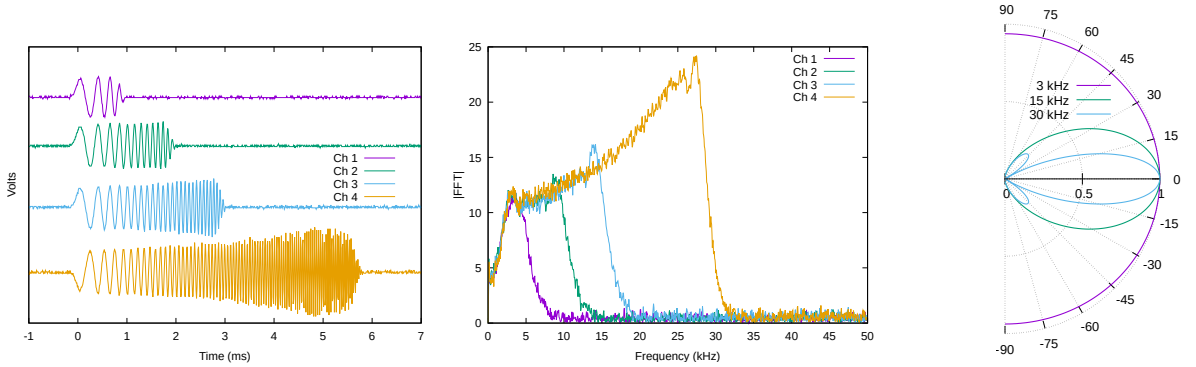

(a) Time signatures (b) Spectra of signals (c) Beam patterns

Figure 8: (a) LFM signals applied to elements of the source array used in several experiments. (b) Fourier transforms of signals in (a). (c) Beam patterns for a 20-cm rectangular aperture.

The TIER model allows for a number of beam patterns to be used in Eq. (1) for the source and receiver. These include beam patterns for rectangular, circular, and omnidirectional apertures as well as the capability to use a tabulated beam pattern from measurement. The beam patterns for rectangular and circular apertures have the general forms [12]:

$$B_r(\omega) = \frac{\sin(kl_h \sin\theta_h)}{kl_h \sin\theta_h} \frac{\sin(kl_v \sin\theta_v)}{kl_v \sin\theta_v}, \tag{14}$$

$$B_c(\omega) = 2\frac{J_1(ka \sin\theta_c)}{ka \sin\theta_c}, \tag{15}$$

respectively. The wavenumber is $k = \omega/c_1$. Horizontal and vertical dimensions of a rectangular aperture are L_h and L_v where Eq. (14) uses $l_h = L_h/2$ and $l_v = L_v/2$; while the radius of the circular aperture is a. With a Cartesian coordinate system centered in the aperture and the acoustic axis aligned with the $\hat{x}$ axis, the angles are defined through $\sin^2\theta_h = y^2/(x^2+y^2)$, $\sin^2\theta_v = z^2/(x^2+z^2)$, and $\sin^2\theta_c = 1 - x^2/(x^2+y^2+z^2)$. For the TIER model simulations, an aperture's Cartesian coordinate system is translated into a target-centered coordinate system, and an Euler-angle rotation is applied to give a properly oriented aperture.

Figure 9 depicts the magnitude of a 6-ms duration LFM pulse where a number of beam patterns are applied in a pitch and catch configuration. The source is fixed and centered on the left axis of each panel at 0°. A receiver is scanned along a path that is parallel to the left axis. In the sub-captions of Fig. 9, the abbreviations 'src', 'rcv', and 'Omni' are used for 'source', 'receiver', and 'omnidirectional', respectively. The separation distance of closest approach between the source and receiver is 10 meters and geometric spread is ignored. It is clear from Fig. 9 that if apodization of an aperture in not applied to a physical source (and/or receiver), then the broad-band response affects the detected scattered pressure from a target.

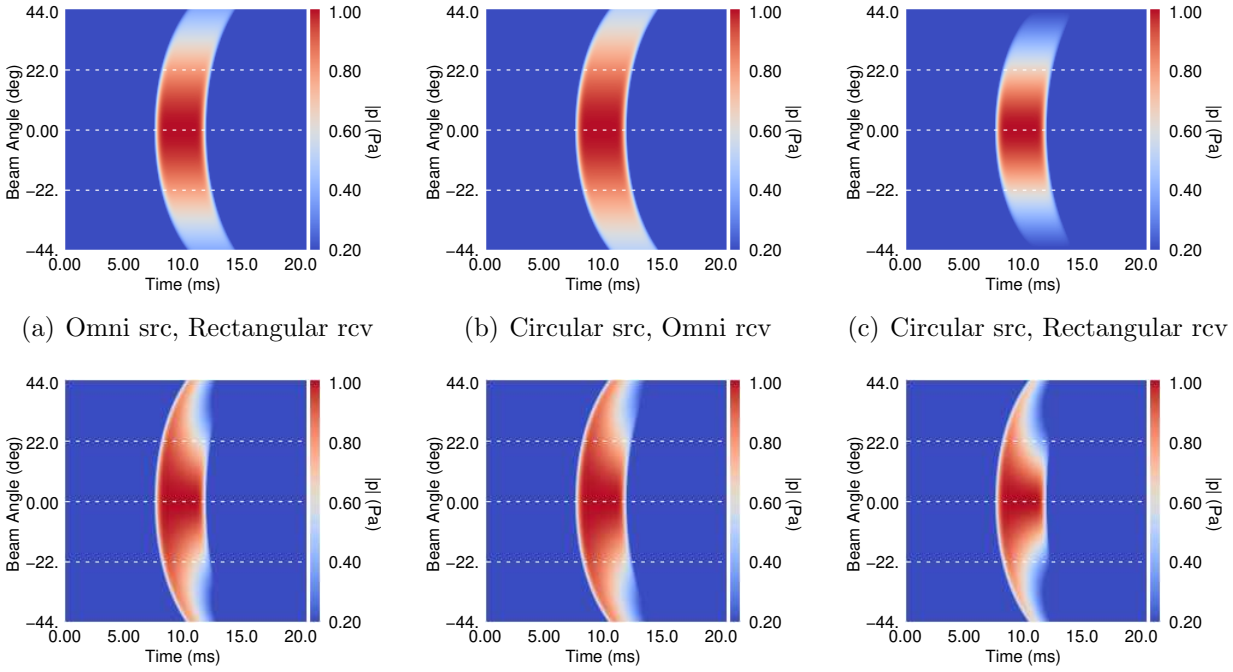

(a) Omni src, Rectangular rcv (b) Circular src, Omni rcv (c) Circular src, Rectangular rcv

(d) Omni src, Rectangular rcv (e) Circular src, Omni rcv (f) Circular src, Rectangular rcv

Figure 9: (a)-(c) Pulse envelops for frequency-independent beam patterns with $k = k_0 \approx 0.64$. (d)-(f) Pulse envelops for frequency-dependent beam patterns with $0.32 < k < 3.2$.

In the classification studies of previous SERDP projects (MR-2231 and MR-2505), APL-UW reduced measured SAS data to acoustic color (AC) templates. An AC template is the absolute target strength as a function of a target-centered aspect angle and frequency. Experimental AC templates were constructed from nine measurements where an isolated target was rotated from $-80°$ to $80°$ in $20°$ increments. (Note, the axis of symmetry of a cylindrical symmetric object is parallel to the SAS rail for a $0°$ orientation.) Overlapping partial AC templates of $\pm 25°$ at each pose angle were merged, where the central $\pm 20°$ range is retained, to generate a full $360°$ AC template. Simulations have been performed to analyze these experiments. The four-element source array of Fig. 8 was simulated by a source with a 10×10 cm^2 aperture. The physical receiver had the same dimensions. For fixed-frequency apertures, the magnitude of the pulse-compressed (PC) signals are depicted in Fig. 10(a), and the corresponding SAS image and AC template are shown in Figs. 10(b) and 10(c). The middle row of Fig. 10 are the results when Eq. (14) is evaluated with its full frequency dependence. The bottom row shows the magnitude of the differences between the top and middle row. The differences in the PC

signals and SAS images are nearly 20 dB down. More importantly, over the ±15° range for the AC template, there is no observed difference down to a -30 dB level.

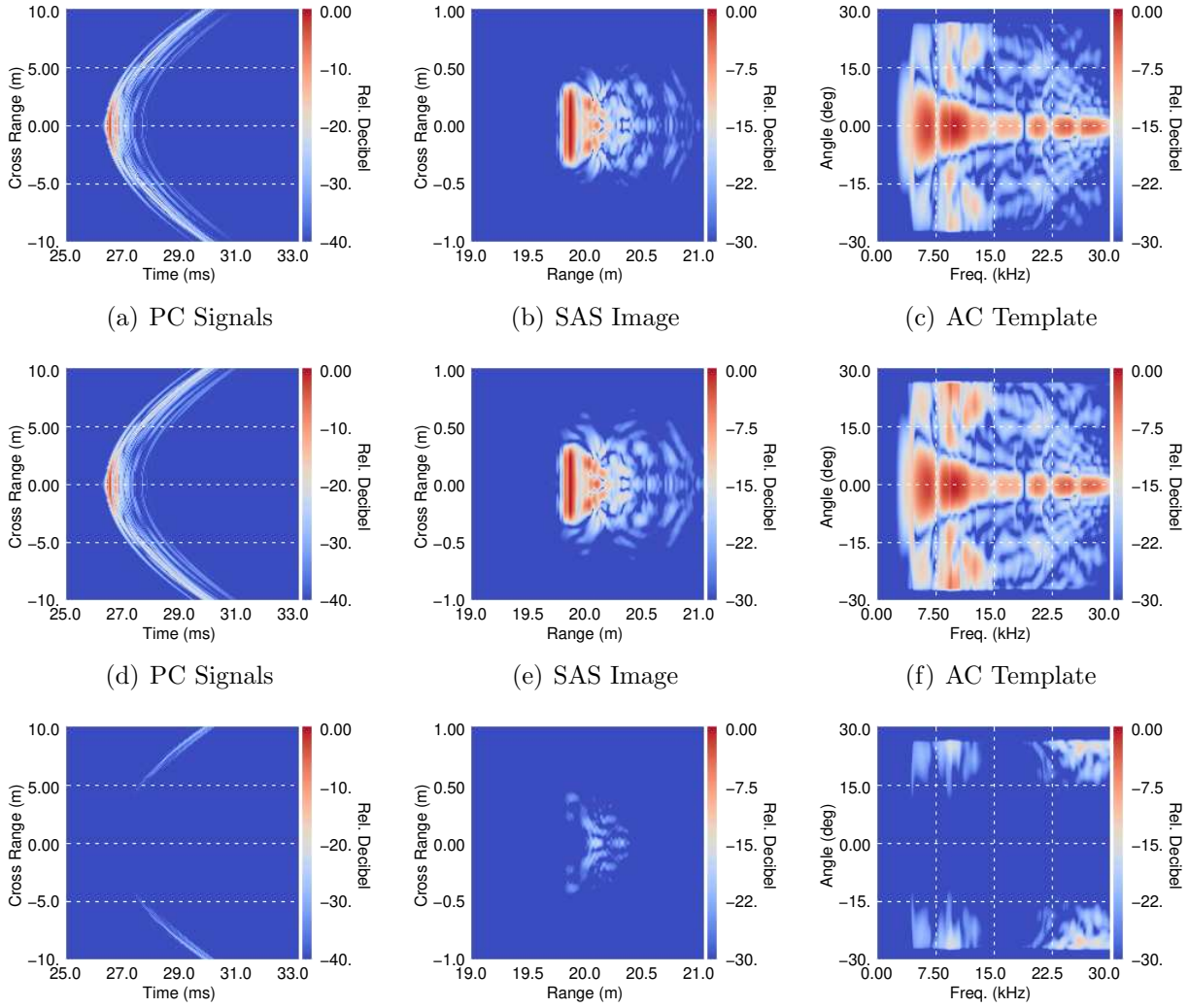

(a) PC Signals (b) SAS Image (c) AC Template

(d) PC Signals (e) SAS Image (f) AC Template

(g) PC Signals (h) SAS Image (i) AC Template

Figure 10: (a) Frequency-independent pulse-compressed signals with carrier frequency of 15 kHz. (b) SAS image generated from time signatures in (a). (c) AC template generated from time signatures in (a). (d) Frequency-dependent pulse-compressed signals with carrier frequency of 15 kHz. (e) SAS image generated from time signatures in (d). (f) AC template generated from time signatures in (d).

5 Reverberation from small-scale surface roughness

The sound scattered from small-scale surface roughness on a water-sediment interface is a primary contribution to reverberation (i.e., background noise). Other contributions to reverberation include noise associated with ships and wind-driven surface waves. Only the reverberation due to small-scale surface roughness is considered here, and is denoted by p_{rev}.

A time-domain reverberation model had been developed, based on first-order perturbation theory, to describe sound scattering from a rough seafloor. A derivation of this model is given in [3, Appendix A]. Several approximations are employed in addition to first-order perturbation theory: the stationary phase approximation is used to evaluate the zero-order field needed for the first-order theory, the sound speed in the sediment is approximated as independent of frequency, the attenuation in the sediment is approximated as linearly increasing with frequency, and the frequency dependence of the source and receive beam patterns is neglected. (Removing the frequency independence will be investigated during the second year of this project.) The latter approximation is reasonably satisfied for APL-UW experiments, because the horizontal aperture of the four-element source is steadily reduced as the frequency is increased by reducing the number of active elements from four down to one in steps (see Sec. 4 and Fig. 8). For bistatic backscattering in the incident vertical plane, this model reduces to the following surface integral over the mean plane of the seafloor:

$$p_{rev}(\boldsymbol{r}_{rcv}, t) = \frac{1}{4\pi c_1^2} \int d^2R \frac{A_{rev}(\boldsymbol{R}) h(\boldsymbol{R}) \ddot{p}_{src}(t - t_{rev})}{|\boldsymbol{r}_{rcv} - \boldsymbol{R}||\boldsymbol{R} - \boldsymbol{r}_{src}|}. \tag{16}$$

The assumed time convention is $\exp(-\imath\omega t)$ with t and ω denoting time and angular frequency. In Eq. (16) the subscript rev denotes quantities related to reverberation, that is, sound scattering from the rough seafloor. Quantities associated with the source and receiver are decorated with src and rcv subscripts. Environmental and system parameters enter through the complex coefficient

$$\begin{aligned} A_{rev}(\boldsymbol{R}) = r_0 B_{src} B_{rcv} \{ & [1 + L(\theta_i)][1 + L(\theta_s)](1 - \kappa^2/\rho) \\ & + (\rho - 1)[1 - L(\theta_i)][1 - L(\theta_s)] \sin\theta_i \sin\theta_s \\ & + (1 - 1/\rho)[1 + L(\theta_i)][1 + L(\theta_s)] \cos\theta_i \cos\theta_s \cos\phi \}, \end{aligned} \tag{17}$$

where B_{src}, B_{rcv}, θ_i, θ_s, and ϕ depend on $\boldsymbol{R} = x\hat{x} + y\hat{y}$. The source and receiver response functions evaluated at $\boldsymbol{R}$ on the mean surface plane are B_{src} and B_{rcv}, and for the development in [3] these functions are evaluated at the carrier frequency of the transmitted LFM signal (i.e., $k \equiv k_0 = \omega_0/c_1$ for Eqs. (14) and (15)). The flat-interface reflection coefficient, $L(\theta)$, is given in Eq. (3), and the incident and scattered grazing angles are determined by $\sin\theta_i = z_{src}/|\boldsymbol{R} - \boldsymbol{r}_{src}|$ and $\sin\theta_s = z_{rcv}/|\boldsymbol{r}_{rcv} - \boldsymbol{R}|$, respectively. The horizontal bistatic angle, ϕ, is the angle between the incident and scattered wave vectors (e.g., $\phi = 0°$ in the forward direction, and $\phi = 180°$ for backscatter). As in Eq. (1), r_0 has been introduced into Eq. (17) to preserve dimensional consistency in Eq. (16). The local height of the seafloor relative to the mean plane is $h(\boldsymbol{R})$, and $p_{src}(t)$ is the pressure field at 1 m from the source on the transmit acoustic axis. The double-dot notation indicates the second partial derivative with respect to time. Finally, the round-trip time delay to propagate from the source to a point $\boldsymbol{R}$ on the mean plane and then back to the receiver is $t_{rev} = (|\boldsymbol{r}_{rcv} - \boldsymbol{R}| + |\boldsymbol{R} - \boldsymbol{r}_{src}|)/c_1$.

The numerical implementation of Eq. (16) has been updated to consider the global coordinate system of the TIER model. This included determination of the proper orientation of the source and receiver apertures within this coordinate system. An example computation for reverberation considered a surface height associated with isotropic small-scale roughness, which is described by the following power law [3]:

$$W(k_x, k_y) = \frac{w_2}{(k_s^2 + k_c^2)^{\gamma_2/2}}. \tag{18}$$

The Cartesian components of the spatial wavenumber $k_s^2 = k_x^2 + k_y^2$ are k_x and k_y, and k_c is a constant cutoff. Figure 11(a) shows a rough surface generated with $w_2 = 0.0016$ m$^{4-\gamma_2}$, $\gamma_2 = 3.82$, and $k_c = 20.9$ m^{-1} (i.e., at a 0.3-m length scale), which fall into the range of values for a medium-fine sand sediment.

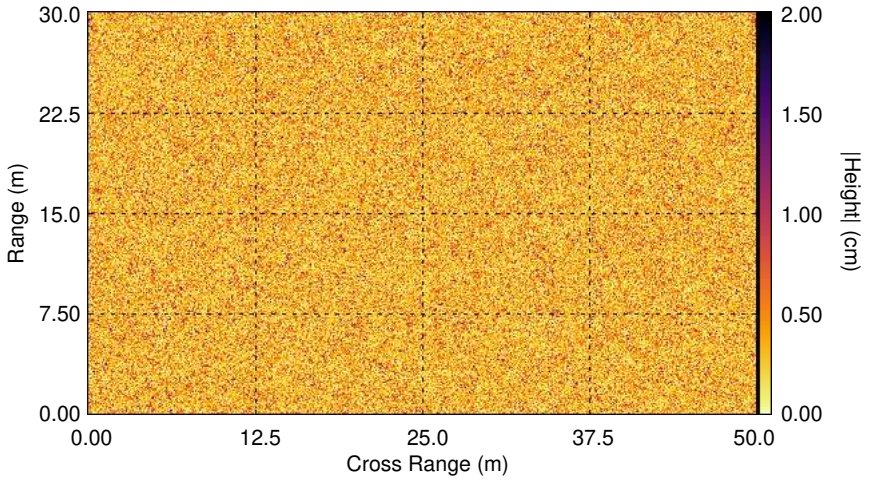

(a) Surface relief

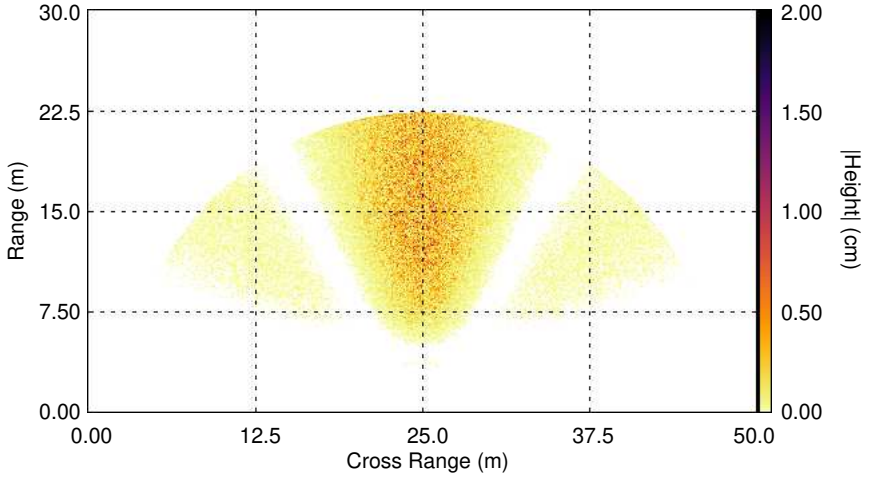

(b) Surface relief weighed by beam patterns

Figure 11: (a) Fourier transform methods allow generation of a random rough surface from Eq. (18). (b) The combination of $h(\boldsymbol{R})$ and $B_{src}B_{rcv}$ from Eqs. (16) and (17) reduces the the computational complexity.

To compute Eq. (16), the double integral is transformed into discrete sums over the mean surface coordinates $\boldsymbol{R}_{m,n} = (m\Delta x, n\Delta y)$. To suppress possible artifacts, the conditions $\Delta x < \lambda/4$ and $\Delta y < \lambda/4$ should be met where λ is the smallest wavelength of interest from the transmitted signal (i.e, $\lambda \approx 5$ cm at 30 kHz). For Fig. 11(a) and $\Delta x = \Delta y = 1$ cm, the discrete sums represents 1.5 million surface points, and by extension, 1.5 million evaluations of Eq. (17). For co-located source and receiver placed at (25,0,5) and a 20° depression angle, the footprint of B_{src} and B_{rcv} on the surface relief is shown in Fig. 11(b). The large semi-circular edge of the footprint is an event horizon associated with the maximum time of the computational window. Thus, the beam patterns and the time window allow a significant reduction in the number of evaluations of Eq. (17) (i.e., on the order of 45 to 50%).

Figure 12 depicts the transmitted signal (also referred to as the replica) and the real part of the reverberation compute from Eqs. (16) and (17). The replica is a tapered 6-ms 1-30 kHz LFM sampled at 100 kHz (i.e., $\Delta t = 10^{-5}$ s), which is often used in the TIER model simulation of APL-UW experiments. Here, the simulation recorded the reverberation in a 8-30 ms time window, where $t = 0$ s is the start of the transmission. As noted above, the semi-circular edge of the footprint shown in Fig. 11(b) is the 30 ms event horizontal. That is, scattering from points on the surface beyond this edge do not enter into this time window. Combining the results for the TIER model, which computes only the target scattering response, and the reverberation model presented here allows one to simulation sonar platforms used in UXO remediation.

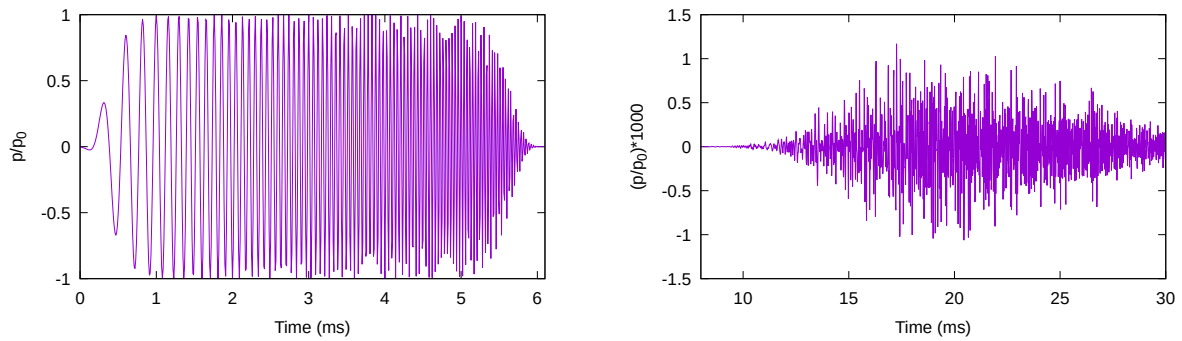

(a) LFM Transmitted Signal

(b) Real Part of Reverberation

Figure 12: (a) The source transmitted a 1-30 kHz LFM signal. (b) The real part of the reverberation computed from Eq. (16) with the surface shown in Fig. 11.

6 Conclusion and Future Work

Progress on SERDP MR19-1234 included the implementation of bistatic scattering for axisymmetric objects, multiple scattering in the free field, frequency-dependent apertures, and updating an older implementation of scattering from a rough surface to account for the background reverberation from the environment. The work on frequency-dependent apertures is complete and reported in Sec. 4. The work on scattering from a rough surface, reported in Sec. 5, utilizes first-order perturbation theory and required an adjustment to use the global coordinate system of the TIER model. The output for the reverberation model was also updated to be compatible with the TIER model.

The work on bistatic scattering from an object concentrated on axisymmetric targets. Symmetry considerations allow the source to be restricted to the xz-plane; while the receiver can be anywhere in space. This then gives a scattering amplitude of the form $s(\theta_s, \theta_r, \varphi_r, \omega)$, which becomes a four-dimensional table, s_{ijkl}. In lieu of one large four-dimensional table, a table is generated for each polar angle of the source, θ_s, where these tables are then three-dimensional in the remaining variables θ_r, φ_r, and f (the actual frequency). Bistatic scattering amplitudes have been generated for the 2:1 aluminum cylinder and a 2:1 aluminum pipe with a 3/8-in wall thickness. The hybrid model has also been use to compute the bistatic scattered pressure from a 105-mm artillery shell. The conversion to a scattering amplitude has yet to be completed. Scattering amplitudes for other axisymmetric targets are to be generated in subsequent work. In particular, Ahmad Abawi from HSL Inc. (San Diego) has been contacted about the generation of the scattered pressure from a finned 105-mm UXO. Targets of this type were deployed in TREX13 and CLUTTEREX17, and cannot be modeled with APL-UW's hybrid model.

CLUTTEREX17 suggested multiple scattering may be an important observable in SAS images from target fields with closely spaced objects. The TIER model has been updated to include the four lowest orders of multiple scattering under free-field scattering. The addition of higher orders has not been pursued, but is a straightforward extension of the method described in Sec. 3. It is noted that multiple scattering requires bistatic scattering, so progress on bistatic scattering inherently impacts multiple scattering. Scattering from an object in a waveguide has been recast into a superposition of free-field scattering problems. Equation (1) covers an object in the free field, in a half-space (e.g., lying proud on a water-sediment interface), in a shallow water environment, and partially and fully buried objects. The methods used to implement multiple scattering in free field will be adapted to other computational components of the TIER model (namely, the half-space component).

In addition to generating additional bistatic scattering amplitudes for objects deployed during CLUTTEREX17 and continuing the investigation on the importance of multiple scattering, a new area of research in the coming year will relax the restriction on an isovelocity environment. The TIER model assumes an isovelocity condition in the water, which means acoustic rays travel in a straight path. Ray tracing models are available for propagation through a stratified ocean such that the sound speed (and possibly density) vary with depth. The BELLHOP model is a well-known ray tracing model, and merging it into the the TIER model will be investigated.

References

[1] S. G. Kargl, A. L. España, K. L. W. J. L. Kennedy, and J. L. Lopes, "Scattering from objects at a wateredi ment interface: experiment, high-speed and high-fidelity models, and physical insight," *IEEE J. Ocean. Eng.*, vol. 40, pp. 632–642, 2015.

[2] L. M. Brekhovskikh and Y. P. Lysanov, *Fundamentals of Ocean Acoustics*, 2nd ed. New York, NY: Springer-Verlag, 1991.

[3] S. G. Kargl, K. L. Williams, and E. I. Thorsos, "Synthetic aperture sonar imaging of simple finite targets," *IEEE J. Ocean. Eng.*, vol. 37, pp. 516–532, 2012.

[4] K. L. Williams, "An effective density fluid model for acoustic propagation in sediments derived from biot theory," *J. Acoust. Soc. Am.*, vol. 110, no. 5, pp. 2276–2281, 2001.

[5] K. L. Williams, S. G. Kargl, E. I. Thorsos, D. S. Burnett, J. L. Lopes, M. Zampolli, and P. L. Marston, "Acoustic scattering from a solid aluminum cylinder in contact with a sand sediment: Measurements, modeling, and interpretation," *J. Acoust. Soc. Am.*, vol. 127, pp. 3356–3371, 2010.

[6] G. C. Gaunaurd and H. Überall, "Rst analysis of monostatic and bistatic acoustic echoes from an elastic sphere," *J. Acoust. Soc. Am.*, vol. 73, pp. 1–12, 1983.

[7] S. G. Kargl and P. L. Marston, "Observations and modeling of the backscattering of short tone bursts from a spherical shell: Lamb wave echoes, glory, and axial reverberations," *J. Acoust. Soc. Am.*, vol. 85, pp. 1014–1028, 1989.

[8] ——, "Ray synthesis of the form function for backscattering from an elastic spherical shell: leaky lamb waves and longitudinal resonances," *J. Acoust. Soc. Am.*, vol. 89, pp. 2545–2558, 1991.

[9] Z. Ye, "A novel approach to sound scattering by cylinders of finite length," *J. Acoust. Soc. Am.*, vol. 102, pp. 877–884, 1997.

[10] T. K. Stanton, "Sound scattering by cylinders of finite length. I. Fluid cylinders," *J. Acoust. Soc. Am.*, vol. 83, pp. 55–63, 1988.

[11] ——, "Sound scattering by cylinders of finite length. II. Elastic cylinders," *J. Acoust. Soc. Am.*, vol. 83, pp. 64–67, 1988.

[12] L. E. Kinsler, A. R. Frey, A. B. Coppens, and J. V. Sanders, *Fundamentals of Acoustics*, 3rd ed. New York: Wiley, 1982.